Displaced fat-jets and tracks to probe boosted right-handed neutrinos in the $U(1)_{B-L}$ model

Rojalin Padhan,[a,b] Manimala Mitra,[a,b] Suchita Kulkarni,[c] Frank F. Deppisch[d]

[a]*Institute of Physics, Sachivalaya Marg, Bhubaneswar, Odisha 751005, India*

[b]*Homi Bhabha National Institute, BARC Training School Complex, Anushakti Nagar, Mumbai 400094, India*

[c]*Institute of Physics, NAWI Graz, University of Graz,Universitätsplatz 5, A-8010 Graz, Austria*

[d]*University College London, Gower Street, London WC1E 6BT, UK*

E-mail: rojalin.p@iopb.res.in, manimala@iopb.res.in, suchita.kulkarni@uni-graz.at, f.deppisch@ucl.ac.uk

ABSTRACT: We investigate the pair-production of Right-Handed Neutrinos (RHNs) via a $B - L$ Z' boson and the detection prospects at the High-Luminosity run of the LHC (HL-LHC) and a future pp collider (FCC-hh). We focus on RHN states with a mass of $10-70$ GeV which naturally results in displaced vertices for small active-sterile mixing strengths. Being produced through a mass resonance with $m_{Z'} \geq 1$ TeV, the RHNs are heavily boosted, leading to collimated decay products that give rise to fat-jets. We investigate the detection prospect of dedicated signatures in the inner detector and the muon spectrometer, namely a pair of displaced fat-jets and the associated tracks, respectively. We find that both the HL-LHC and FCC-hh can be sensitive to small active-sterile mixing $V_{\mu N} > 10^{-6}$ and $V_{\mu N} > 10^{-7}$ with the number of events reaching $\mathcal{O}(10)$ and $\mathcal{O}(10^3)$, respectively. This allows probing the generation of light neutrino masses through the Seesaw mechanism in this scenario.

Contents

1 Introduction

The discovery of the Standard Model (SM) like Higgs boson at the Large Hadron Collider (LHC) experiment has proven that in the SM, masses of the fermions and gauge bosons are generated via the Brout-Englert-Higgs (BEH) mechanism. However, the origin of light neutrino masses and mixing still remains a key question, which can not be explained by the SM. A number of neutrino oscillation experiments have observed that, the solar and atmospheric neutrino mass splittings are $\Delta m_{12}^2 \sim 10^{-5}$ eV^2 and $\Delta m_{13}^2 \sim 10^{-3}$ eV^2, and the mixing angles are $\theta_{12} \sim 32°$, $\theta_{23} \sim 45°$, and $\theta_{13} \sim 9°$ [1]. There have been a number of proposed beyond the Standard Model (BSM) extensions, which can explain the observed light neutrino masses and mixings and contain SM gauge singlet right-handed neutrinos (RHNs). The $U(1)_{B-L}$ model is such an extension, where the gauge sector is also extended by an additional $U(1)_{B-L}$ gauge group [2–5]. The model contains three right handed neutrinos N_i, which are SM gauge singlet, however carry non-trivial charges under the $U(1)_{B-L}$ gauge symmetry. Other than the three RHNs, the model also contains an extended gauge sector, and a complex scalar S. The SM neutrino mass in this model is generated

from the lepton number violating (LNV) $d = 5$ seesaw operator $LLHH/\Lambda$ [6, 7] via Type-I seesaw mechanism [8–12].

Being SM gauge singlet RHNs interact with the SM particles only via their mixing with the active neutrinos, referred as active-sterile mixing, which is proportional to $\sqrt{m_\nu/M_N}$, where m_ν and M_N are the light neutrino and the RHN mass scales, respectively. Since $m_\nu <$ eV, this mixing is small for RHN with mass few tens to hundreads of GeV, leading to an in-general suppressed production of a single RHN at a pp collider. This limitation can however be evaded in the gauged $B - L$ model, since RHNs can be produced via additional production mechanism that involves unsuppressed interactions of RHN with BSM/SM particles [13, 14].

Motivated by this, we study pair-production of RHNs in gauged $B - L$ model, where the production primarily occurs via mediation of BSM gauge boson Z'. Specifically, we focus on the low mass region of N satisfying $M_N < M_W$, for which N gives rise to distinctive model signatures. The produced N undergoes three body decays to few different final states, among which we consider $N \to \mu qq'$ decay mode. For the considered mass range, two body decay of N is kinematically forbidden. Since the decay of N strongly depends on the active-sterile mixing, hence for mixing in agreement with eV light neutrino mass, the RHN undergoes displaced decays where its decay vertex is considerably displaced from the production vertex. Additionally, due to a large hierarchy between the masses of the Z' and N, the decay product of N is collimated, resulting in a displaced *fat-jet* signature. We hence study distinctive long-lived signatures of N, that can be detected at the High-Luminosity upgrade of the LHC, and the future FCC-hh machine. For previous studies on displaced RHN decay, see [15–21].

In particular, we consider displaced decays of N in two different region of the detectors, a) in the inner detector (ID) and b) the farthest end of the detector, which is muon spectrometer (MS). To realise the former, N must have proper decay length ranging between $\ell \sim$ mm to hundreds of mm, while for later, the decay length should be $\ell \sim$ m. We note that the signal description between a) and b) differ widely. For the decay of N in ID, the signature contains two displaced *fat-jets*. For N decaying in the MS, the track properties in the ID, energy deposits in the calorimeter can not be used, which are used for the jet formation. Therefore, a jet description of the final state particles is inadequate in this case, and we instead perform a track-based analysis. We further extend the analysis by demanding displaced decay of at-least one RHN in the ID/MS. Assuming a background free environment we find that few tens of displaced *fat-jet* events can be observed at the HL-LHC for c.m.energy $\sqrt{s} = 14$ TeV and luminosity $\mathcal{L} = 3\,\mathrm{ab}^{-1}$. For FCC-hh that can operate with a much higher c.m.energy $\sqrt{s} = 100$ TeV and luminosity $\mathcal{L} = 30\,\mathrm{ab}^{-1}$, the maximum achievable events increases by order of magnitude. For the decay of N in the MS, the discovery prospect at the HL-LHC is rather low. This however improves significantly for FCC-hh.

The discussion proceeds as follows: In Section. 2, we present a brief review of the model, following which we present a discussion on existing constraints in Section. 3. In Section. 4, and Section. 5, we discuss the displaced decays and pair-production of two Ns. We present an extensive analysis for HL-LHC and FCC-hh in Section. 6 and Section. 7, respectively.

Finally, we present a summary in Section. .

2 The $B - L$ gauge model

We consider the gauge $B - L$ model, which in addition to the particles of the SM sector also contains three right-handed neutrinos ν_R, a BSM Higgs field S and a BSM gauge boson B'_μ. The gauge group is $SU(3)_c \times SU(2)_L \times U(1)_Y \times U(1)_{B-L}$, where the scalar and fermionic fields S and ν_{Ri} have $B - L$ charges $B - L = +2$ and -1, respectively. The SM states have the conventional $B - L$ charges. Here, the field S represents a complex scalar field, which acquires vacuum expectation value (vev) $v_{BL} \neq 0$ and breaks the $B - L$ gauge symmetry. The states ν_{Ri} contribute to the light neutrino mass generation via the seesaw mechanism. The complete Lagrangian of the model has the form

$$\mathcal{L} = \mathcal{L}_{SM} + \mathcal{L}_{B-L}, \tag{2.1}$$

where $\mathcal{L}_{B-L}$ is the $B - L$ Lagrangian, and $\mathcal{L}_{SM}$ is the Lagrangian for the SM sector. The $B - L$ Lagrangian has the form

$$\mathcal{L}_{B-L} = \left(D_\mu S\right)^\dagger \left(D^\mu S\right) - \frac{1}{4} F_{BL\mu\nu} F_{BL}^{\mu\nu} + i\bar{\nu}_{Ri}\gamma^\mu D_\mu \nu_{Ri} - V_{B-L}\left(\phi, S\right)$$
$$- \sum_{i=1}^3 y^M S \bar{\nu}_{Ri}^c \nu_{Ri} - \sum_{i,j=1}^3 y_{ij}^\nu \bar{L}_i \tilde{\phi} \nu_{Rj} + h.c. \,, \tag{2.2}$$

with

$$V_{B-L}\left(\phi, S\right) = \mu_S^2 S^\dagger S + \mu_\phi^2 \phi^\dagger \phi + \lambda_1 \left(\phi^\dagger \phi\right)^2 + \lambda_2 \left(S^\dagger S\right)^2 + \lambda_3 \left(\phi^\dagger \phi\right)\left(S^\dagger S\right). \tag{2.3}$$

In the above, D_μ represents the covariant derivative [22],

$$D_\mu = \partial_\mu + ig_s \mathcal{T}_\alpha G_\mu^\alpha + igT_a W_\mu^a + ig_1 Y B_\mu + i(\tilde{g}Y + g'Y_{B-L})B'_\mu, \tag{2.4}$$

where G_μ^α, W_μ^a, B_μ are the SM gauge fields with associated couplings g_s, g, g_1 and the respective generators are $\mathcal{T}_\alpha$, T_a, Y, respectively. The field denoted as B'_μ represents the gauge field for $U(1)_{B-L}$ gauge symmetry, g' represents the respective gauge coupling and the $B - L$ quantum number is denoted by Y_{B-L}. In this paper, we neglect the mixing between $U(1)_{B-L}$ and $U(1)_Y$ to simplify the model, i.e. we consider the minimal gauged $B - L$ model. This model is therefore valid in the limiting case of small mixing between B_μ and B'_μ. The gauge sector of the model also includes the following kinetic term for the gauge field B'_μ,

$$\mathcal{L}_{kin}^{BL} = -\frac{1}{4} F'^{\mu\nu} F'_{\mu\nu}, \tag{2.5}$$

where $F'_{\mu\nu} = \partial_\mu B'_\nu - \partial_\nu B'_\mu$ is the field strength tensor of the $B - L$ gauge group. The kinetic term for the RHN and the SM fermion fields are

$$\mathcal{L} = i\overline{\nu_{Ri}}\gamma_\mu D^\mu \nu_{Ri} + i\overline{\psi_i}\gamma_\mu D^\mu \psi_i \tag{2.6}$$

In the above, ψ represents the SM fermion fields. These fields receive an additional term in their covariant derivatives, since they are non-trivially charged under the $B - L$ gauge symmetry, with $Y_{B-L} = 1/3$ and -1 for the quark and lepton fields, respectively. In the above a summation over the fermion species and generations is implied.

- *Neutrino mass:* In Eq. (2.2), the Yukawa matrix y^ν represents the Dirac Yukawa coupling and y^M is the Yukawa coupling connecting the RHNs with the complex scalar field S. The RHN mass is generated due to breaking of the $B - L$ symmetry, with the mass matrix given by $M_R = y^M \langle S \rangle$. The light neutrinos mix with the RHNs via the Dirac mass matrix $m_D = y^\nu v / \sqrt{2}$. The complete mass matrix in the (ν_L, ν_R^c) basis has the form

$$\mathcal{M} = \begin{pmatrix} 0 & m_D \\ m_D^T & M_R \end{pmatrix}, \tag{2.7}$$

  where

$$m_D = \frac{y^\nu}{\sqrt{2}} v, \quad M_R = \sqrt{2} y^M v_{BL}. \tag{2.8}$$

  Here, $v = \langle \phi^0 \rangle$ and $v_{BL} = \langle S \rangle$ are the vacuum expectation values for electroweak and $B - L$ symmetry breaking, respectively. In the seesaw limit, $M_R \gg m_D$, the light and heavy neutrino masses are

$$m_\nu \sim -m_D M_R^{-1} m_D^T, \quad M_N \sim M_R. \tag{2.9}$$

  The flavour and mass eigenstates of the light and heavy neutrinos are connected as

$$\begin{pmatrix} \nu_L \\ \nu_R^c \end{pmatrix} = \begin{pmatrix} V_{ll} & V_{lN} \\ V_{Nl} & V_{NN} \end{pmatrix} \begin{pmatrix} \nu_L^m \\ N_R^c \end{pmatrix}, \tag{2.10}$$

  where ν_L^m and $(N_R^c)^T$ represent the left-chiral mass basis for the light and heavy neutrinos, respectively. In our subsequent discussion, we represent the physical Majorana fields for the light and heavy neutrinos via $\nu^m = \nu_L^m + (\nu_L^m)^c$ and $N = N_R + (N_R)^c$, respectively. In the above, we schematically write the 6-dimensional mixing matrix in terms of 3-dimensional blocks. Assuming the charged lepton mass matrix to be diagonal, the sub-block V_{ll} can approximately be considered as the PMNS mixing matrix U_{PMNS}. The other sub-block V_{lN} represent the mixing between the light and RHN states and is referred as active-sterile mixing. In general, V_{lN} is an arbitrary 3×3 matrix. However, to pursue a collider study on the proposed signature, it is sufficient for us to consider one generation of RHNs and only non-zero $V_{\mu N}$, which we follow in the subsequent sections.

- *Z' Gauge boson mass:* Due to the presence of an additional $U(1)_{B-L}$ gauge symmetry, the model contains BSM gauge bosons B'_μ. We refer to the massive state as Z'. Similar to the RHNs, the additional neutral gauge boson mass $M_{Z'}$ is generated via

spontaneous breaking of $B - L$ gauge symmetry. The mass of Z' is related to the symmetry breaking scale v_{BL} as

$$M_{Z'} = 2g' v_{BL}, \tag{2.11}$$

where g' is the associated $B - L$ gauge coupling constant.

- *SM Higgs and BSM Higgs:* After spontaneous symmetry breaking (SSB), the SM Higgs doublet ϕ and BSM scalar S is given by

$$\phi = \begin{pmatrix} 0 \\ \dfrac{v + h_1}{\sqrt{2}} \end{pmatrix}, \quad S = \left(\dfrac{v_{BL} + h_2}{\sqrt{2}} \right), \tag{2.12}$$

with the dynamical states h_1 and h_2. Owing to the non-zero λ_3, h_1 and h_2 mix with each other which leads to the scalar mass matrix given by

$$\mathcal{M}_{\text{scalar}}^2 = \begin{pmatrix} 2\lambda_1 v^2 & \lambda_3\, v_{BL}\, v \\ \\ \lambda_3\, v_{BL}\, v & 2\lambda_2 v_{BL}^2 \end{pmatrix}. \tag{2.13}$$

The basis states h_1 and h_2 can be rotated by suitable angle α to the new basis states H_1 and H_2. The new basis states represents the physical basis states which are given by,

$$H_1 = h_1\, \cos\alpha - h_2\, \sin\alpha, \tag{2.14}$$
$$H_2 = h_1\, \sin\alpha + h_2\, \cos\alpha, \tag{2.15}$$

where H_1 is the SM-like Higgs and H_2 is the mostly BSM Higgs. The mixing angle between the two states is

$$\tan 2\alpha = \frac{v v_{BL} \lambda_3}{v^2 \lambda_1 - v_{BL}^2 \lambda_2}. \tag{2.16}$$

The mass square eigenvalues of H_1 and H_2 are given by,

$$M_{H_1, H_2}^2 = \lambda_1 v^2 + \lambda_2 v_{BL}^2 \pm \sqrt{(\lambda_1 v^2 - \lambda_2 v_{BL}^2)^2 + (\lambda_3 v v_{BL})^2}. \tag{2.17}$$

In what follows, we consider the scalar mixing to be negligible, for which the SM and BSM Higgs masses have the form, respectively

$$M_{H_1} \sim \sqrt{\lambda_1} v, \quad M_{H_2} \sim \sqrt{\lambda_2} v_{BL} \tag{2.18}$$

Due to this choice of small mixing, any BSM Higgs production and its decay to two RHNs will be suppressed.

The RHNs have charged current and neutral current interactions with the SM fields, with the scalars H_1, H_2 and the gauge boson Z'. The respective charged current interaction Lagrangian has the form,
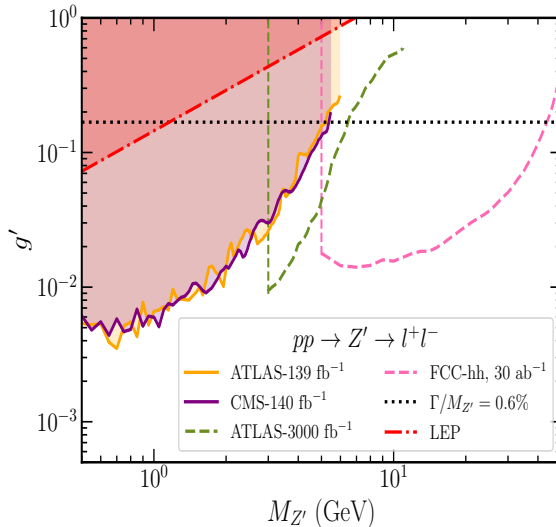
Figure 1: Limits in the $M_{Z'}$ and g' plane derived from ATLAS [23], and CMS [24] searches. The limit from LEP-II [25] has been shown by the dot-dashed red line. The green dashed and orange dashed lines represent the projection for HL-LHC [26] and FCC-hh [27], respectively. The black horizontal dotted line represents $\Gamma/M_{Z'} = 0.6\%$.

$$-\mathcal{L}_{CC} = \frac{g}{\sqrt{2}} W_\mu^- \bar{\ell}\gamma^\mu \nu_\ell + \text{H.c.} = \frac{g}{\sqrt{2}} W_\mu^- \bar{\ell}\gamma^\mu \left(V_{ll}P_L\nu_l^m + V_{lN}P_L N\right) + \text{H.c.,} \qquad (2.19)$$

where P_L is the left-chirality projection operator $P_L = \frac{1-\gamma^5}{2}$. Similarly, the NC interaction is given by

$$\begin{aligned}
-\mathcal{L}_{NC} &= \frac{g}{2\cos\theta_w} Z_\mu \bar{\nu}_\ell \gamma^\mu \nu_\ell + g' Z'_\mu \bar{\nu}_R \gamma^\mu \nu_R \\
&\approx \frac{g}{2\cos\theta_w} Z_\mu \left[\bar{\nu}_i^m \gamma^\mu P_L \nu_i^m + \{(V_{ll}^\dagger V_{lN})_{ij}\bar{\nu}_i\gamma^\mu P_L N_j + \text{H.C.}\}\right] + g' Z'_\mu \bar{N}_i \gamma^\mu P_R N_i,
\end{aligned}$$

$$(2.20)$$

In the above, i, j represent generation indices. The interaction with the SM and BSM Higgs have the form

$$\mathcal{L}_{int}^N = y^M \cos\alpha \; \bar{N} H_2 N + y^M \sin\alpha \; \bar{N} H_1 N + \left[V_{ll}^\dagger V_{lN} \cos\alpha \; \nu^{\bar{m}} H_1 N + H.C.\right]. \qquad (2.21)$$

3 Experimental constraints

The Z' and N of the gauged $B - L$ model are significantly constrained from the non-observation of any direct signature at LEP, and LHC. In addition, eV light neutrino masses impose additional constraints on the model parameters. Below we briefly summarise the different existing constraints,

- **Heavy resonance search:** the search for a massive resonance at LHC decaying to di-lepton/di-jet imposes tight limits on the respective production cross-section. The
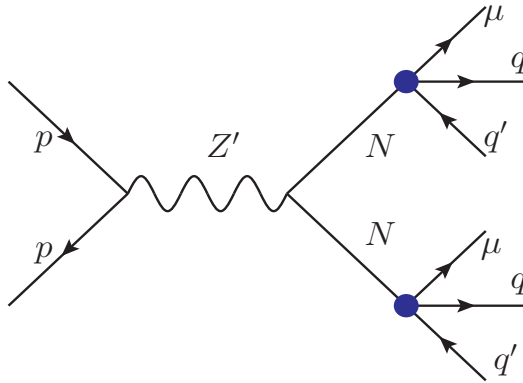
Figure 2: Feynman diagram representing pair-production of two RHNs via Z' mediation and its displaced decays to a lqq' final states.

13 TeV LHC search for a heavy resonance decaying into two leptons $pp \to Z' \to l^+l^-$ put a constraint $M_{Z'} > 5.0$ TeV at 90% C.L, assuming a 100% branching ratio of Z' decaying into two leptons. For different branching ratios, the limit relaxes. In Fig. 1, we translate the di-lepton constraint from the LHC on $M_{Z'}$, and g' plane. We adopt the following procedure in translating the bound. For the ATLAS search with $\mathcal{L} = 139 \, \text{fb}^{-1}$, we consider $\sigma^{\text{th}}(pp \to Z' \to l^+l^-) < \sigma_{obs}$, where the observed limit corresponds to the stringent 95% C.L. limit from [23]. The CMS limit is set on the relative cross section, $\sigma^{\text{rel}} = \frac{\sigma \times Br^{\text{obs}}\big|_{Z'}}{\sigma \times Br^{\text{obs}}\big|_Z} \times 1928 \, \text{pb}$. Therefore, to obtain the 95% C.L. limit on $\sigma \times Br^{\text{obs}}\big|_{Z'}$ we fold σ^{rel} with $\sigma \times Br^{\text{obs}}\big|_Z/1928$ pb. Here, $\sigma \times Br^{\text{obs}}\big|_Z$ is the observed cross section in the $m_{l^+l^-} = 60 - 120$ GeV window, which can be calculated as $N^{\text{obs}}/(\text{Acc} \times \text{Eff} \times \mathcal{L})$[1]. In Fig. 1, we represent the $ee + \mu\mu$ combined limit by the purple line from the CMS search and the orange line represents the limit from the ATLAS search. As we consider the results for $\Gamma/M_{Z'} = 0.6\%$ for the CMS search, we show this by black horizontal dotted line. The dashed green line represents the future sensitivity of HL-LHC with 3000 fb^{-1} [26] and the dashed magenta line represents projection for FCC-hh [27] . We also note that the former search at LEP-II [25, 28–30] for a massive resonance constrains Z' mass and gauge coupling, and thus the $B - L$ breaking scale as $v_{BL} \equiv M_{Z'}/(2g') \geq 3.45$ TeV. It has been shown by the dashed red line, which is considerably relaxed w.r.t. the present LHC limit.

- **Search for RHN:** Other than the constraint on Z', the RHN mass and mixings are also constrained, both from neutrino mass measurements as well as direct searches at the LHC. In the present work, we consider relatively low mass RH neutrinos, 10 GeV $< M_N < M_W$, which are mainly produced from the Z' mediated channel. The RHN mass and its mixing with the active neutrinos are tightly constrained from

---

[1]For the di-electron (di-muon) channel $N^{\text{obs}} = 28194452$ (164075), Acc $\times$ Eff= 0.176 (0.073) and $\mathcal{L} =137$ (140) fb^{-1} [24].

light neutrino mass measurements. As we are working with a Type-I seesaw scenario with $B - L$ gauge symmetry, the light neutrino mass $m_\nu \simeq m_D^2/M_R \simeq V_{lN}^2 M_N$ where the active-sterile mixing angle $V_{lN} \simeq m_D/M_R$. This fixes the active-sterile mixing,

$$V_{lN} \approx 10^{-6} \sqrt{\frac{m_\nu/(0.1 \text{ eV})}{M_N/(50 \text{ GeV})}}. \tag{3.1}$$

The low mass RHN is further constrained by LHC searches for a heavy neutral lepton [31] via the decay mode $pp \to W \to lN$ and the decay $N \to ll\nu/ljj$. The search for a displaced neutral lepton [31, 32] in particular constrains active-sterile mixing as $V_{\mu N} < 10^{-2}$ for RHN mass $\mathcal{O}(10)$ GeV. Other searches such as [33–35] mainly target heavier masses, where the RHN is not displaced, and hence not relevant for our case.

- **LLP searches from SM Higgs decay:** there are different exotic decays of the SM Higgs boson which give rise to distinctive signatures. The decay $H_1 \to NN$ followed by the decay of N into $ljj/ll\nu$ final states give rise to displaced lepton/displaced jet signature, as in the mass range of interest N has a large decay length. The decay is open kinematically, however it has a very suppressed branching ratio due to our choice of a small α. The partial decay width of this decay mode has the form

$$\Gamma(H_1 \to NN) = \frac{3 M_{H_1} y^{M2} \sin^2 \alpha}{8\pi} \left(1 - \frac{4M_N^2}{M_{H_1}^2}\right)^{3/2}, \quad \text{where} \quad y^M = \frac{M_N}{\sqrt{2} v_{BL}}. \tag{3.2}$$

For instance, the branching ratio $\text{BR}(H_1 \to NN)$ becomes 0.005% for $\sin\theta = 3 \times 10^{-3}$ and $M_N = 50$ GeV. There are different CMS and ATLAS searches [36–39] to probe exotic decays of the SM Higgs into two LLP states, which can be compared with. This includes a search for exotic decays of the Higgs boson into LLP in the tracking system [36–39], or a search for LLP decaying in the ATLAS muon spectrometer [40–42], and in the CMS endcap muon detectors [43]. Due to a very suppressed branching ratio, M_N and V_{lN} are unconstrained from these searches.

4 Pair production and decay of RHN at a pp machine

The RHN can be pair produced via the processes $q\bar{q} \to Z' \to NN$ and $q\bar{q} \to H_1/H_2 \to NN$, among which the Higgs mediated channels give suppressed cross-sections, as we consider a small SM-BSM Higgs mixing $\sin\alpha$. Therefore, production in pair primarily occurs via $pp \to Z' \to NN$ channel. The cross-section depends strongly on the gauge coupling g', the mass of Z' gauge boson $M_{Z'}$, its decay width $\Gamma_{Z'}$, as well as the mass of the RHN M_N. We show the respective Feynman diagram for this process in Fig. 2.

In the left and right panel of Fig. 3, we show the pair production cross-section of RHN, $\sigma(pp \to Z' \to NN)$ as a function of $M_{Z'}$ at the HL-LHC and FCC-hh, respectively. This cross-section is calculated using MadGraph. For illustration, we assume two different values of couplings, $g' = 0.1, 0.003$ and $M_N = 20$ GeV. We show the LHC constraints (as shown in Fig. 1) by the black solid and dotted lines for g' values 0.1 and 0.003, respectively. For
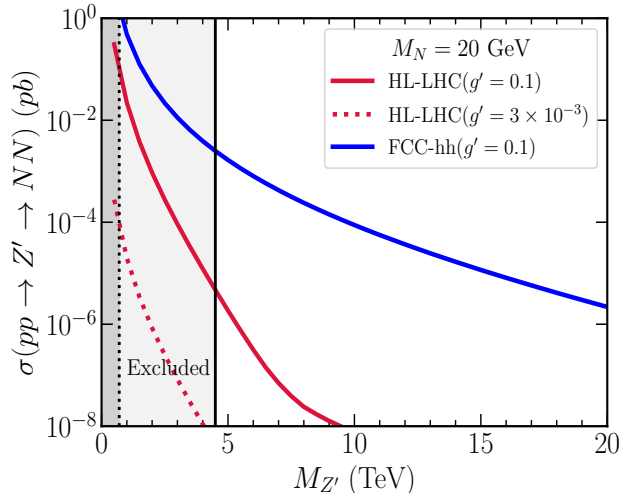
Figure 3: Cross-section $\sigma(pp \to Z' \to NN)$ as a function of $M_{Z'}$ at the HL-LHC and FCC-hh, for $M_N = 20$ GeV. Black solid (dashed) line represents LHC limits for $g' = 0.1$ (3×10^{-3}) as shown in Fig. 1.

instance, for the choice of gauge coupling $g' = 0.003$, the heavy resonance search in l^+l^- decay channel rules out any value of $M_{Z'} \lesssim 0.7$ TeV. For $g' = 0.1$ the exclusion limit reaches higher value, $M_{Z'} \gtrsim 4.5$ TeV. Since in this figure we consider $M_{Z'}$ satisfying $M_{Z'} > 2M_N$, the on-shell production of Z' and its decay will dominate the pair-production cross-section $\sigma(pp \to NN)$. As can be seen from the figure, for the same gauge coupling g', the ratio of cross-section $\mathcal{R} = \sigma(pp \to NN)_{HL-LHC}/\sigma(pp \to NN)_{FCC-hh}$ vary over a wide range. For on-shell Z' production with narrow width approximation $\Gamma_{Z'}/M_{Z'} \simeq 10\%$, or less, this can be expressed as,

$$\sigma(pp \to NN)_{HL-LHC}/\sigma(pp \to NN)_{FCC-hh} \approx \sigma(pp \to Z')_{14}/\sigma(pp \to Z')_{100} \quad (4.1)$$

With an increase in the c.m. energy from $\sqrt{s} = 14$ TeV to 100 TeV, the ratio $\mathcal{R}$ increases by order of magnitude, and the increase is larger for higher masses. This occurs as the partonic c.m. energy is larger in a 100 TeV collider compared to the available partonic c.m. energy for 14 TeV.

We also show the variation of cross-section for HL-LHC and FCC-hh w.r.t. the variation of both M_N and $M_{Z'}$ in Fig. 4. For this figure we consider the same values of gauge coupling that we use for Fig. 3 The shaded vertical region show the present constraint from LHC, both in the left and right panel. In the figure of left panel, the cross-section is significantly suppressed for $M_N > M_{Z'}/2$, as can be seen from the figure. This happens as Z' is not on-shell in this region. For Z' with mass $\sim$ TeV and $M_N \ll M_{Z'}$, the cross-section can be in the sub-fb range. From the figure of right panel, this can be seen, that for higher Z' mass the production cross section is almost independent of the mass of RHN for the variation of $M_N = 100$ GeV to 2 TeV.

Decay of RHN: The RHN interacts with a lepton and a W gauge boson, which is governed by the active-sterile mixing V_{lN}. It also interacts with light neutrino and a Z, H_1,
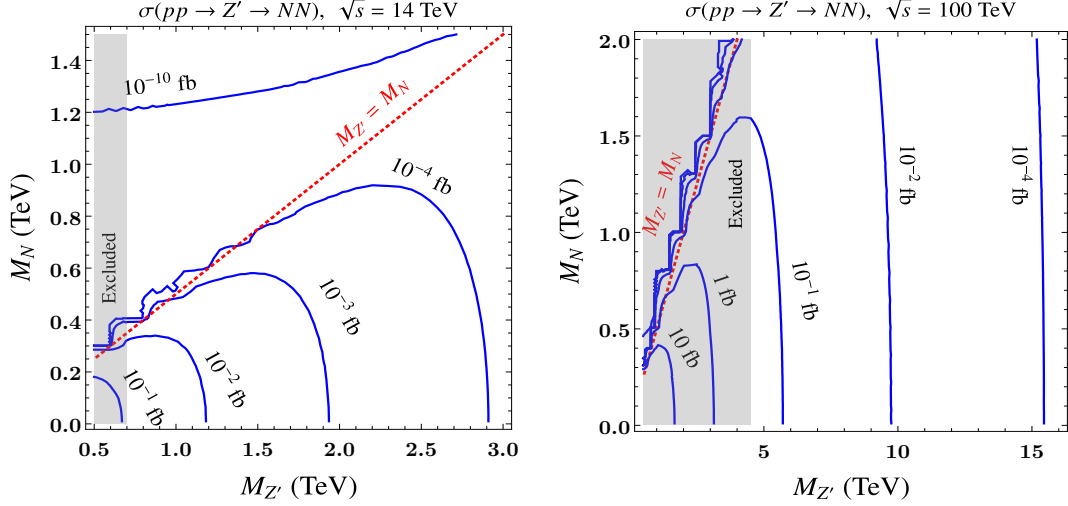
Figure 4: Cross-section $\sigma(pp \to Z' \to NN)$ as a function of M_N and $M_{Z'}$. Left: For $g' = 0.003$ and c.m. energy $\sqrt{s} = 14$ TeV. Right: For $g' = 0.1$ and c.m. energy $\sqrt{s} = 100$ TeV. The vertically shaded region represents the LHC exclusion limit.

as well as, Z' and BSM Higgs H_2. For the mass range being considered in this work $M'_Z, M_{H_2} \gg M_W, M_Z, M_{H_1} > M_N$, the RHN N decays pre-dominantly via an off-shell W, Z, H_1 states into two SM fermions. The two body decay of RHN into a $(lW, \nu Z, \nu H_{1,2})$ state will only open if mass of N larger than the two body kinematic limit. The partial decay widths for $N \to lqq'$, $\nu f\bar{f}$ and $\nu\nu\nu$ decay modes have the following expressions [44],

$$\Gamma(N \to l_\alpha^- u\bar{d}) = N_c|V_{ud}^{CKM}|^2|V_\alpha|^2 \frac{G_F^2 M_N^5}{192\pi^3} \mathcal{I}(x_u, x_d, x_l) \tag{4.2}$$

In the above, $\mathcal{I}(x_u, x_d, x_l) = 12 \int_{(x_d+x_l)^2}^{(1-x_u)^2} \frac{dx}{x}(1+x_u^2-x)(x-x_d^2-x_l^2)\lambda^{\frac{1}{2}}(1, x, x_u^2)\lambda^{\frac{1}{2}}(x, x_l^2, x_d^2)$, $x_{u/d/l} = \frac{m_{u/d/l}}{M_N}$, $\lambda(a, b, c) = a^2 + b^2 + c^2 - 2ab - 2bc - 2ca$, and $N_c = 3$ is the color factor. The partial decay width for $N \to l_\alpha^- \nu_\beta l_\beta^+$ with generation index $\alpha \neq \beta$ have the following expression,

$$\Gamma(N \to l_\alpha^- \nu_\beta l_\beta^+) = |V_\alpha|^2 \frac{G_F^2 M_N^5}{192\pi^3} \mathcal{I}(x_{l_\alpha}, x_{l_\beta}, x_{\nu_\beta}) \tag{4.3}$$

The partial decay width for the other mode with a same $\alpha = \beta$ is given by,

$$\Gamma(N \to \nu_\alpha f\bar{f}) = N_c|V_\alpha|^2 \frac{G_F^2 M_N^5}{192\pi^3}\left[C_1^f\left((1 - 14x^2 - 2x^4 - 12x^6)\sqrt{1-4x^2} + 12x^4(x^4-1)L(x)\right) + \right.$$
$$\left. 4C_2^f\left(x^2(2+10x^2-12x^4)\sqrt{1-4x^2} + 6x^4(1-2x^2+2x^4)L(x)\right)\right] \tag{4.4}$$

Here $x = \frac{m_f}{M_N}$, $L(x) = \log\left[\frac{1-3x^2-(1-x^2)\sqrt{1-4x^2}}{x^2(1+\sqrt{1-4x^2})}\right]$. The values of C_1^f and C_2^f are given in [44].

$$\Gamma(N \to \nu\nu\nu) = |V_\alpha|^2 \frac{G_F^2 M_N^5}{96\pi^3} \tag{4.5}$$

In addition to this there can also be two body decays $N \rightarrow l^{\pm} \pi^{\pm}$, however, this is suppressed in our case, as we consider $M_N > 1$ GeV $\sim$ the scale of non-perturbative QCD. Therefore, we do not consider this channel in our analysis. For $M_N = 10 - 70$ GeV, the dominant decay mode is $N \rightarrow \mu j j$ with a branching ratio BR($N \rightarrow \mu j j$) $\simeq 0.5$. Branching ratios for other decay modes are BR($N \rightarrow \nu j j$) $\simeq 0.2$, BR($N \rightarrow \nu_\mu l^+ l^-$) $\simeq 0.10$, BR($N \rightarrow \mu e \nu_e + \mu \tau \nu_\tau$) $\simeq 0.15$ and BR($N \rightarrow \nu \nu \nu$) $\simeq 0.05$.

5 RHN decay in inner tracker and muon spectrometer

We are interested in a signature which contains a pair of RHNs produced from Z' decay and the decay of N to a $N \rightarrow l q q'$ final state. To be specific, we consider the $N \rightarrow \mu q q'$ final state and analyse the model signature. Signatures with an electron in the final state $N \rightarrow e q q'$ can also potentially be explored by similar search strategies. Specifically, we consider two scenarios: (a) when the N decays within the inner detector (ID) of the HL-LHC/FCC-hh, and (b) in the muon spectrometer (MS). The search strategies for these two different decay modes differ widely. We will also consider a combination of these two, when one RHN decays in the ID and other in the MS. In order to analyse the model signatures, we simulate the events using the following steps. We use the FeynRules [45, 46] model file and Universal FeynRules Output (UFO) [47] corresponding to Ref. [15], which we use in combination with the Monte Carlo event generator `MadGraph5aMC@NLO` -v2.6.7 [48] to generate events at the parton level. The FeynRules [45, 46] model file and UFO is publicly available from the FeynRules Model Database at [49]. For every signal sample, we generate 50000 signal events with `MadGraph5aMC@NLO` -v2.6.7, where we use NN23LO1 PDF set [50]. We set max jet flavour at 5 to take account of the b quark contribution in the PDF. We then pass the generated parton level events on to PYTHIA v8.235 [51] which handles the initial and final state radiation, parton showering, hadronization, and heavy hadron decays. The clustering of the events and jet formation are performed by FastJet v3.2.1 [52]. We consider a Cambridge-Aachen jet algorithm [53] for jet clustering with radius parameter $\mathcal{R} = 1.0$. We analyse events at the generator level with PYTHIA v8.235.

5.1 Decay Probability of N

For $M_N < M_W$ and for the viable range of active-sterile mixing that satisfies light neutrino mass constraint, the RHN N undergoes displaced decays with a displacement $l \sim mm$ or even longer. N decays via off-shell W, Z, H states with the decay length [2]

$$\tau_N \simeq 25 \times \left(\frac{10^{-6}}{|V_{\mu N}|} \right)^2 \times \left(\frac{100 \text{ GeV}}{M_N} \right)^5 \text{ mm} \tag{5.1}$$

In Fig. 5, we show the distribution of the decay length of N in the lab frame for $\sqrt{s} = 14$ TeV and $\sqrt{s} = 100$ TeV for few benchmark values of $M_{Z'}$, and M_N, which we later on use in the analysis. For this distribution we generate $pp \rightarrow Z' \rightarrow NN$ in MadGraph, and to keep the information of decay length, use the decay-in-flight option of MadGraph. As can

---

[2]The contribution from the Higgs in partial decay width is an order of magnitude smaller and hence we do not consider this.
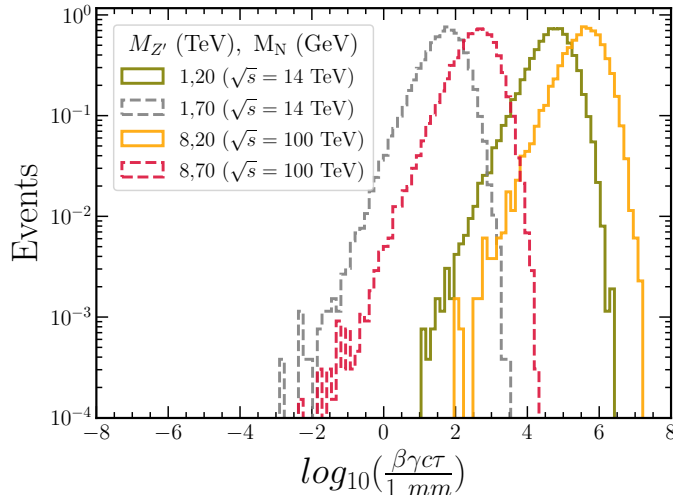
Figure 5: Distribution of the decay length of N at the HL-LHC and at FCC-hh for the considered masses of Z' and N.

be seen, in the majority of events, decay length of N is more than a mm, thereby giving rise to a decay vertex considerably displaced from the production vertex of N.

As we have two RHNs from the channel $pp \to Z' \to NN$, therefore the two RHNs can decay in different parts of the HL-LHC and FCC-hh detectors. The probability that both the RHNs decay within a distance interval (L_1, L_2) from their production vertex is given by

$$\mathcal{P}(L_1, L_2, \sqrt{s}, M_N, M_{Z'}, \theta) = \int db_1 db_2 \ f(\sqrt{s}, M_N, M_{Z'}, b_1, b_2) \prod_{i=1}^{2} \left[e^{\frac{-L_1}{b_i c\tau(\theta)}} - e^{\frac{-L_2}{b_i c\tau(\theta)}} \right] \quad (5.2)$$

where $c\tau$ is proper decay length, θ represents the active-sterile mixing and $b_{1,2} = (\beta\gamma)_{1,2}$ are the boost factors of the two RHNs. and $f(\sqrt{s}, M_N, M_{Z'}, b_1, b_2)$ is the probability distribution function of the boost. The probability that one RHN decay within interval (L_1, L_2) and the other within interval (L_3, L_4) is given by

$$\mathcal{P}(L_1, L_2, L_3, L_4, \sqrt{s}, M_N, M_{Z'}, \theta) = 2 \times \int db_1 db_2 \ f(\sqrt{s}, M_N, M_{Z'}, b_1, b_2) \left[e^{\frac{-L_1}{b_1 c\tau(\theta)}} - e^{\frac{-L_2}{b_1 c\tau(\theta)}} \right] \times$$
$$\left[e^{\frac{-L_3}{b_2 c\tau(\theta)}} - e^{\frac{-L_4}{b_2 c\tau(\theta)}} \right] \quad (5.3)$$

The decay probability of one RHN decaying within length $L_1 - L_2$ then becomes,

$$\mathcal{P}(L_1, L_2, \sqrt{s}, M_N, M_{Z'}, \theta) = \int db \ f(\sqrt{s}, M_N, M_{Z'}, b) \left[e^{\frac{-L_1}{bc\tau(\theta)}} - e^{\frac{-L_2}{bc\tau(\theta)}} \right] \quad (5.4)$$

where b is the boost factor of the respective RHN. We use the boost distributions of N from the HepMC file [54], which has been generated by showering the LHE events [55] from MadGraph.

To estimate the probability of decay of N in various parts of the HL-LHC and FCC-hh detectors, we adopt a simplistic approach. In Table. 1, we present the fiducial volume

Detector Geometry		
	HL-LHC	FCC-hh
Inner detector (ID)	(2-300) mm	(25-1550) mm
Calorimeter (CAL)	(2000-4000) mm	(2700-4700) mm
Muon Spectrometer (MS)	(4000-7000) mm	(6000-9000) mm

Table 1: Coverage of geometric acceptance of various sub-detectors of the HL-LHC and FCC-hh.
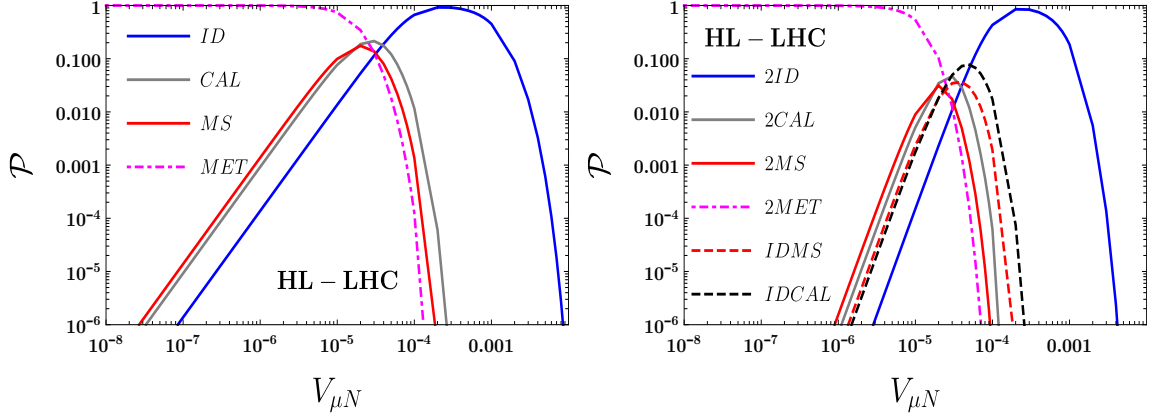

Figure 6: Decay probability of one RHN (left) and two RHN (right) in different parts of the HL-LHC detector. For this figure, we consider $M_N = 20$ GeV, $M_{Z'} = 1$ TeV. ID, MS, CAL and MET represent the decay of N in the inner detector, muon spectrometer, calorimeter and outside of the detector, respectively. In the right panel, IDMS (IDCAL) represents the joint probability of one N decaying in the ID and the other decaying in the MS (CAL).

of the sub-detectors, where the decay of RHN leads to observable signatures. For Inner detector (ID) we demand RHN decays in between 2 mm and 300 mm. In this region, the vertex reconstruction efficiency is large [41]. The decays of RHN in ID leads to multi-track displaced vertex. Similar to ID the decay of N in the MS creates a number of tracks. For this we consider that RHN decays within 4000-7000 mm where muon ROI trigger efficiency is higher [42]. Hadronic decays of RHN in the outer edge of the ECal or in the HCal leads to a distinct signatures marked by significantly large energy deposit in HCal compared to that in the ECal [56]. We however do not consider such signature in the present analysis, rather restrict to RHN decay in ID and in MS. For the FCC-hh detector coverage of various sub-detectors used in the analysis, we refer the readers FCC-CDR [57].

In Fig. 6, we show the probability of the RHNs decaying in different modules of the HL-LHC detector. The left panel represents the decay probability of a single N in the detector and in the right panel, we show the probability for both the Ns to undergo displaced decays. The acronyms ID, CAL, MS, MET refer to the decay of RHN inside the inner detector, the calorimeter, the muon spectrometer, and outside of the CMS and ATLAS detector,

respectively. From the figure, it is evident that the probability is maximal if the RHN decays inside the inner detector or outside of the detector, and it is minimal, if the decay happens in the muon spectrometer. The probability for other configurations, such as if the decay occurs in the calorimeter, or among the two Ns one decays in the inner detector and another in calorimeter/muon spectrometer is somewhat in between. We show the respective probabilities for the FCC-hh in Fig. 7.

Fig. 6 and Fig. 7 illustrate useful information about the respective geometric probabilities of the RHN to undergo displaced decays. A naive comparison between the results derived for HL-LHC and FCC-hh shows that while the maximum decay probability of one/two N decaying within ID is very similar $\simeq 95\%$, the probability for one N decaying in the ID and the other in MS is somewhat larger in FCC-hh than HL-LHC. A large probability along with a higher c.m. energy and a higher achievable integrated luminosity will result in a significantly large number of events, that can be observed at the FCC-hh. In the subsequent sections, we present a detailed discussion of the observable signal events at HL-LHC and FCC-hh, while taking into account both the kinematic and geometric cut efficiencies.
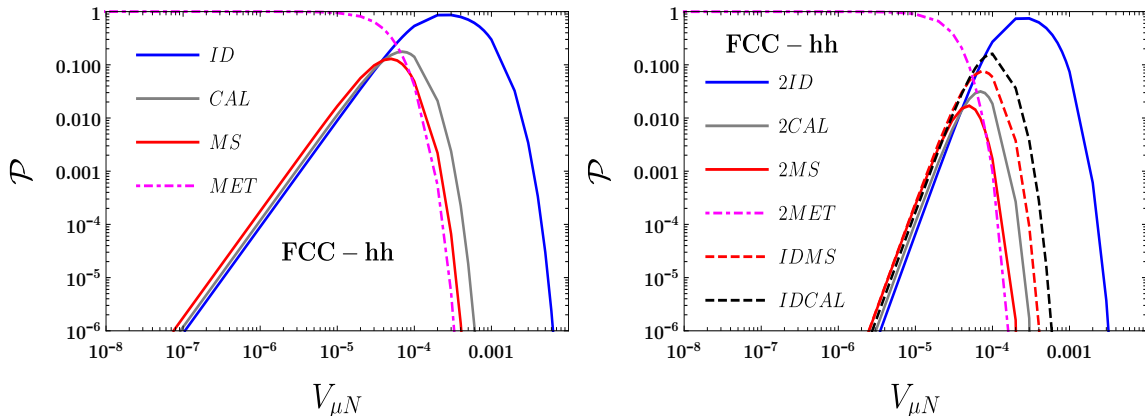

Figure 7: As Fig. 6 but shows the decay probability for the FCC-hh detector with $M_N = 20$ GeV and $M_{Z'} = 8$ TeV.

5.2   Signal description for N decaying in the ID

As we are focussing on a heavier Z' with mass $M_{Z'} \geq 1$ TeV, and lighter N with masses $10 - 70$ GeV satisfying $M_N < M_W$, the N hence will be boosted, resulting in collimated decay products[3]. In Fig. 8, we show the $\Delta R = \sqrt{(\Delta\eta)^2 + (\Delta\phi)^2}$ separation between the muon and the closest quark at the parton level, originating from the decay of a RHN. The ΔR separation between two closest quarks also shows similar features. As can be seen, in most of the events the muon-quark separation $\Delta R(\mu, q) \ll 0.4$, where $\Delta R = 0.4$ has often been utilised in experimental analyses as the isolation criterion between final states. Instead of abiding by the selection criterion with jet radius $\mathcal{R} = 0.4$ and standard isolation criterion

---

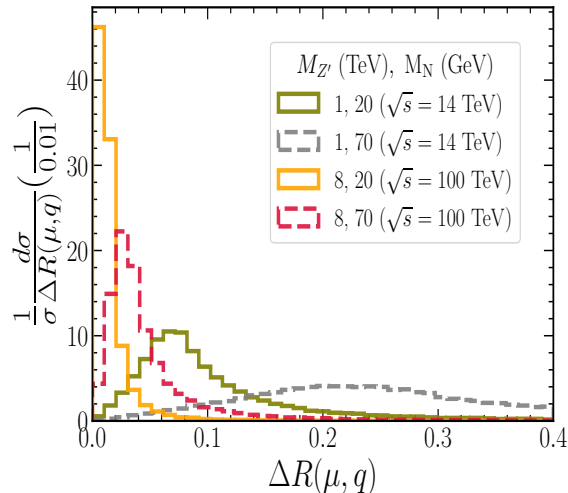[3]$M_N < 10$ GeV is not motivated due to more SM background for displaced vertex signatures.

Figure 8: ΔR separation between the μ and closest q at the partonic level.

$\Delta R(\ell, j), \Delta R(j, j) > 0.4$, we hence demand a large jet radius $\mathcal{R} = 1.0$, referred to as *fat-jet* [58]. Since we consider a large jet-radius and do not impose any specific isolation criterion, in the majority of the events, the lepton hence will be part of the *fat-jet*. Extending further, we also show the distributions of ΔR after jet clustering. In left panel of Fig. 9, we show the ΔR separation of the closest μ from the leading jet, for both $\sqrt{s} = 14$ TeV and $\sqrt{s} = 100$ TeV. It is evident from the figure that the ΔR separation between the μ and the j is $\Delta R(\mu, j) \ll 0.4$, which mimics the partonic distribution, shown in Fig. 8.

As we have pointed out before, for the considered RHN state with mass $M_N < M_W$, the eV scale light neutrino mass demands a very suppressed active-sterile mixing $V_{lN} \sim 10^{-6}$, thereby leading to a macroscopic decay length for N. Therefore, the final state originating from $pp \rightarrow Z' \rightarrow NN$ decay would be

- $pp \rightarrow Z' \rightarrow NN \rightarrow \underbrace{\mu j j} \quad \underbrace{\mu j j} \rightarrow J_{fat}^{dis} \quad J_{fat}^{dis}$

In the above J_{fat}^{dis} represents the *fat-jet* originating from N decay, which is also displaced. Since the *fat-jet* is formed by the decay products of N, which is considerably lighter than Z', satisfying $\frac{M_N}{M_{Z'}} \ll 1$, the N and hence the leading and sub-leading jet have a high transverse momentum. We show the p_T distribution of leading and sub-leading jets in the right panel of Fig. 9. As can be seen, for $M_{Z'} = 1$ TeV and $M_N = 20$ GeV, the distribution peaks around $p_T \sim M_{Z'}/2 = 500$ GeV. For $M_{Z'} = 8$ TeV, the peaks appear at a higher value, $p_T \sim M_{Z'}/2 = 4$ TeV. This high transverse momentum of leading and sub-leading jets will be useful in designing the selection cuts.

We also note that the proposed signal can also be extended to include ejj final state. This however depends strongly on the active-sterile mixing V_{eN}. With $V_{eN} \ll V_{\mu N}$, the contribution from ejj channel will be small. Here, we adopt a simplistic approach and consider only $V_{\mu N} \neq 0$, therefore do not consider ejj state in *fat-jet* description.
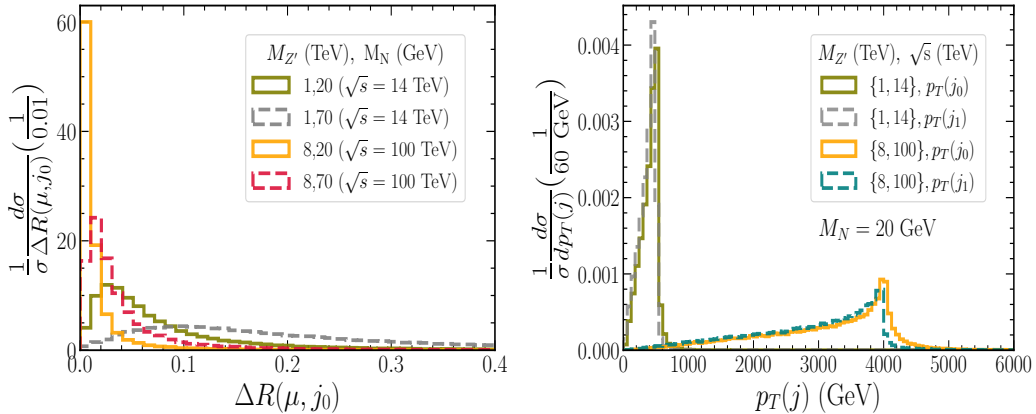
Figure 9: Left: ΔR separation between the μ and leading jet. Right: Transverse momentum distribution of the leading and sub-leading fat-jet.

5.3 Signal description for N decaying in the MS

If the RHN decays within the muon spectrometer, then one can not use the information on the number of tracks in the ID, p_T of track, and other variables such as deposited energy in the calorimeter. Instead of performing an analysis based on observables of a *fat-jet*, we rather present a track based analysis. The final state originating from $pp \to Z' \to NN$ would be considered as

- $pp \to Z' \to NN \to \underbrace{\mu q q'}\ \underbrace{\mu q q'} \to \mu^{dis}\mu^{dis} + X^{dis} \to \underbrace{track_1 + track_2 + ...track_n} + \underbrace{Y}$

where μ^{dis} represents a muon, produced from the RHN displaced decays. In the above, X corresponds to all other final state particles, including hadrons, electrons, photons etc. which are generated due to RHN decays as well as due to showering. We represent all the charged particles generated from the decay of RHN as $track_1, track_2, ..track_n$ and Y represent any neutral particle in the final state that does not leave any footprint of a charged track in the muon spectrometer.

For these above mentioned model signatures, we first perform the analysis for HL-LHC with c.m. energy $\sqrt{s} = 14$ TeV considering an integrated luminosity $\mathcal{L} = 3\,\mathrm{ab}^{-1}$ and later investigate the discovery prospect for FCC-hh with $\sqrt{s} = 100$ TeV with $\mathcal{L} = 30\,\mathrm{ab}^{-1}$. To evaluate the number of events for the above mentioned two signal descriptions, we implement both the geometric and kinematic cuts, the details of which are provided in Section. 6, and Section. 7. The geometric cuts take into account the probability of RHN to decay within a specified region of HL-LHC/FCC-hh detector. For the geometric cut efficiency, we follow the prescription described in Section. 5.1, and use Eq. (5.2), Eq. (5.3), and Eq. (5.4). As kinematic cuts, we use following few variables - p_T of jet, p_T of associated tracks, η of jet and tracks. Below, we briefly outline the adopted procedure, which we implement for the analysis:

- We implement both kinematic and geometric cuts to evaluate the number of signal events that can be detected. Let g and k denote the geometric and kinematic cuts.

We denote the corresponding probabilities for an event to pass g and k by ϵ_g and ϵ_k, respectively, and $\epsilon_{g\&k}$ is the probability that an event pass both g and k. The probability that an event known to pass the kinematic cuts k, will also pass g is given as (using conditional probability),

$$\epsilon_{g|k} = \epsilon_{g\&k}/\epsilon_k. \tag{5.5}$$

To evaluate the above, we use the boost distribution of RHN, undergoing displaced decays. In Eq. (5.2), Eq. (5.3), and Eq. (5.4), we consider that $f(\sqrt{s}, M_N, M_{Z'}, b_1, b_2)$ is the boost distribution of Ns from those events that satisfy the kinematic cut. We evaluate the geometric cut-efficiency using the above-mentioned equations and the kinematic cut-efficiencies has been calculated in PYTHIA v8.235 [51]. With this, we obtain

$$\epsilon_{g|k} = \mathcal{P}(L_1, L_2, \sqrt{s}, M_N, M_{Z'}, \theta). \tag{5.6}$$

Using Eq. (5.5), the final cut-efficiency including both the geometric and kinematic cuts becomes

$$\epsilon_{g\&k} = \epsilon_{g|k} \times \epsilon_k = \mathcal{P}(L_1, L_2, \sqrt{s}, M_N, M_{Z'}, \theta) \times \epsilon_k, \tag{5.7}$$

where the probability $\mathcal{P}$ in the above has been simulated from the event samples that satisfy the kinematic cuts.

The cross-sections after cut for the two signal descriptions are evaluated as

$$\sigma(pp \to NN \to J^{dis}_{fat} J^{dis}_{fat})\big|_{after-cut} = \sigma_p \times \mathcal{P}(L_1, L_2, \sqrt{s}, M_N, M_{Z'}, \theta) \times \epsilon_k, \tag{5.8}$$

and

$$\sigma(pp \to NN \to \underbrace{track_1 + ..track_n}_{} + \underbrace{Y}_{})\big|_{after-cut} = \sigma_p \times \mathcal{P}(L_1, L_2, \sqrt{s}, M_N, M_{Z'}, \theta) \times \epsilon_k, \tag{5.9}$$

where $\mathcal{P}(L_1, L_2, \sqrt{s}, M_N, M_{Z'}, \theta)$ and ϵ_k represent the corresponding geometric and kinematic cut-efficiencies for RHN decay, respectively. In the above, σ_p is the partonic cross-section for $pp \to Z' \to NN \to \mu jj \mu jj$. We have explicitly checked that the cut-efficiencies following this procedure match with the cut-efficiencies obtained with a full Pythiav8.235 based numerical simulation with a mismatch $< \mathcal{O}(5\%)$.

6 Projection for HL-LHC

To evaluate the discovery prospect of N, which decays in the inner detector/muon spectrometer of the HL-LHC detector, we use kinematic variables - transverse momentum p_T and pseudo-rapidity $|\eta|$ of jets, and p_T, $|\eta|$ of tracks. We first obtain the results demanding displaced decays of two Ns, which give distinctive signatures with low background. This is referred as 2IDvx or 2MSvx events, depending on whether N decay in the ID or in MS. We also show the projection relaxing the tight requirement of exact two displaced vertices, and analyse the signature with at least one N undergoing displaced decay (referred as 1IDvx, and 1MSvx events). Note that all the results are calculated under the zero background assumption. For the HL-LHC analysis we consider $M_{Z'} = 1$ TeV, $g' = 0.003$.
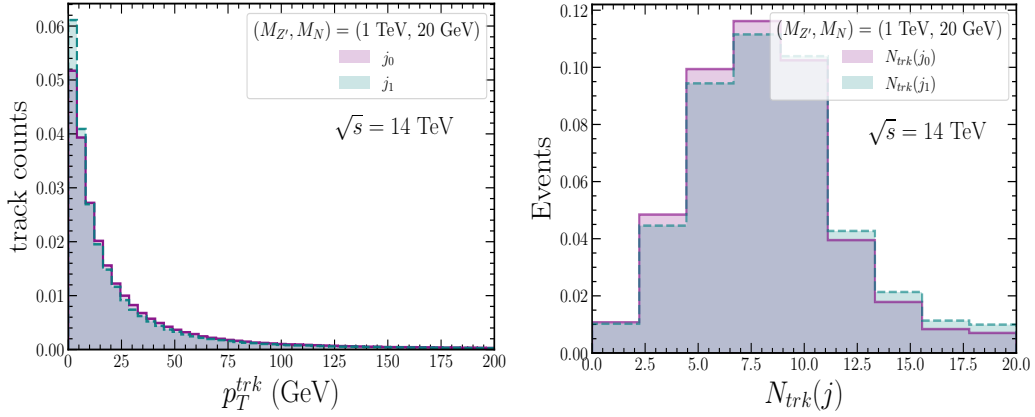
Figure 10: Left panel: p_T of tracks associated to leading and sub-leading jets. Right panel: number of tracks associated to $j_{0,1}$ for HL-LHC.
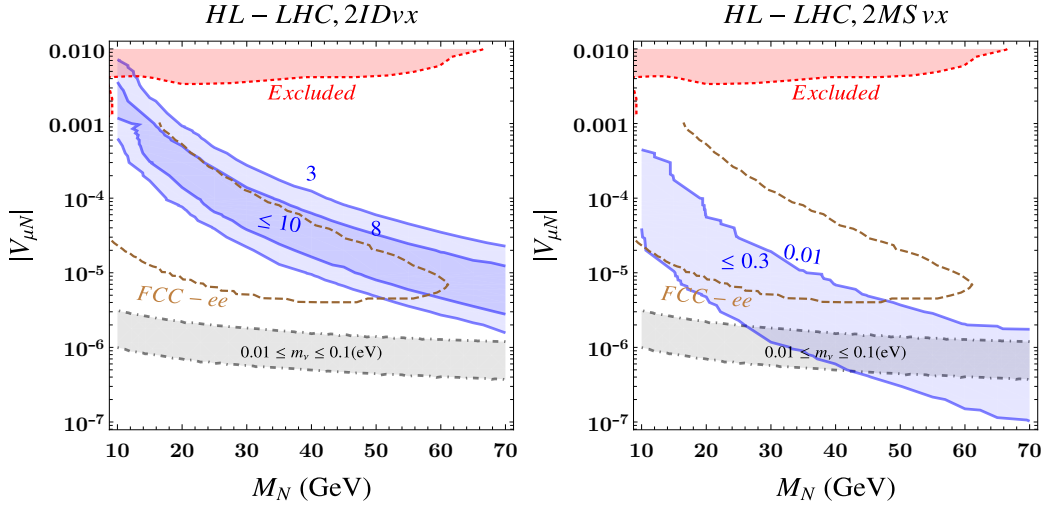

Figure 11: Contours of 2IDvx (left) and 2MSvx (right) events that can be achieved with $\mathcal{L} = 3\,\text{ab}^{-1}$. A maximum of $N_{events} = 10$ events can be observed in 2IDvx event category. The brown dashed line represents the FCC-ee projection [59, 60], and the red shaded region represents the excluded region from [61, 62].

6.1 Decay vertex in the inner-detector (IDvx):

We consider the following sets of cuts for the analysis of two displaced vertices in the ID,

- *C1:* Both the RHN decay within $ID_{L_1} = 2$ mm and $ID_{L_2} = 300$ mm.

- *C2:* The leading and sub-leading fat-jet $j_{0,1}$ has to satisfy $|\eta(j)| < 4.5$ and $p_T(j) \geq 150$ GeV. The strong cut on jet-p_T is motivated by the ATLAS analysis of boosted RHN [63] and other fat-jet analyses [64, 65].

- *C3:* Additionally for each of the leading and sub-leading fat-jet, number of associated track with $p_T \geq 1$GeV, $|\eta| < 2.5$ should be $n_{trk} \geq 4$. This can be easily satisfied,

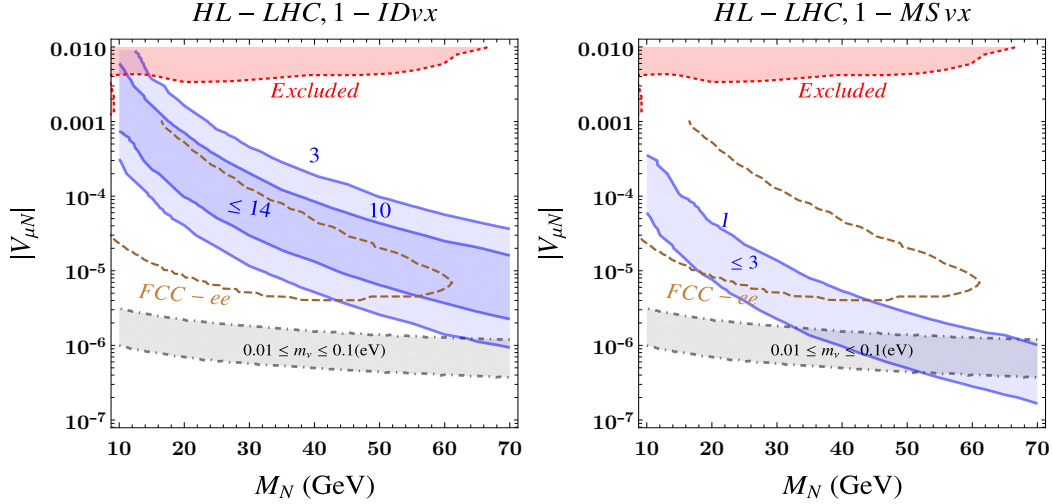**Figure 12**: Contours of 1IDvx (left) and 1MSvx (right) events with $\mathcal{L} = 3\,\mathrm{ab}^{-1}$ at the HL-LHC.

as majority of events have a $p_T(track) > 1$ GeV, as is evident from the left panel of Fig. 10. The number of tracks associated to the leading and sub-leading jet peaks around ~ 7, hence the selection criterion on number of tracks is easily satisfied. These criteria are inspired from the ATLAS search for long-lived particles decaying into displaced hadronic jets in ID [41].

- *C4:* Finally we select the events if number of jets $n_j \geq 2$ and the above-mentioned cuts are satisfied for both the leading and sub-leading *fat-jets*.

As we outline in Section. 5.1, we consider the boost distribution of the two Ns from the events that satisfy the above mentioned kinematic cuts *C2-C4* and evaluate the geometric cut-efficiency as $\mathcal{P}(L_1, L_2, \sqrt{s}, M_N, M_{Z'}, \theta)$ using Eq. 5.2, and Eq. 5.3. In the left panel of Fig. 11, we show the contours for $N_{events} = 3$ and 8 events in $|V_{\mu N}|$ and M_N plane by blue solid lines. A maximum number of 10 2IDvx events can be observed with the luminosity $\mathcal{L} = 3\,\mathrm{ab}^{-1}$. In the same plot, we also show the projection for FCC-ee in the channel $e^+ e^- \to Z \to \nu N$ by the brown dashed line, derived in [59, 60]. The region shaded in red is excluded from CMS and ATLAS searches in both prompt and displaced leptonic decay signatures of RHNs [60–62]. We also show the active-sterile neutrino mixing required for light neutrino mass m_ν in between $0.01 - 0.1$ eV.

We also estimate the number of events demanding decay of at least one N in the ID [4] and show the result in the left panel of Fig. 12. For this, we consider only the probability of one RHN decay within $2 - 300$ mm using Eq. 5.4 and the kinematic cut-efficiencies as $\epsilon_k \sim 100\%$. We checked explicitly that more than 90% events satisfy the above mentioned kinematic cuts. With the requirement of at least one N decaying in the ID, the probability is slightly larger, which leads to maximum number of events as $N_{events} = 14$, that can be obtained with $3\,\mathrm{ab}^{-1}$ of data.

---

[4]The other N can decay in any region of the detector, and we are not tagging its decay.

6.2 Decay vertex in the muon spectrometer (MSvx):

We consider that N has a long lifetime and it decays to $\mu q q'$ in the muon-spectrometer. We consider the following sets of selection cuts:

- *C1:* We demand both the RHN decay occur within the muon-spectrometer between the length $MS_{L_1} = 4000$ mm, and $MS_{L_2} = 7000$ mm. The chosen length interval corresponds to the outer edge of the HCal and the middle station of muon chambers where the muon RoI trigger efficiency is higher [42].

- *C2:* For each of the tracks originating from RHN decay vertex we impose $p_T(track) > 1$ GeV, $|\eta(track)| < 2.7$ and $n_{trk} \geq 4$.

- *C3:* Finally we select the events if two decay vertex and the associated tracks from the vertex satisfy the above selection criterion. We also demand $\Sigma_{track} P_T(track) > 60$ GeV, which along with the cut $n_{trk} \geq 4$ ensures a significant number of hits in the muon-spectrometer.

We evaluate the geometric cut-efficiencies following Eq. 5.2 and Eq. 5.3 using the event samples that satisfy selection cuts *C2-C3*. The kinematic and geometric cuts have been designed based on the ATLAS searche [42]. In the right panel of Fig. 11, we show the number of events for the 2MSvx events. We also show the number of events demanding decay of at least one N in the muon spectrometer in the right panel of Fig. 12, where we consider only the geometric cut-efficiency. The notable difference between the 2IDvx events and 2MSvx events is that the number of events in the later case reduces significantly. This can be understood by referring Fig. 6, where we show the probability of two N decaying in different region of the HL-LHC detector. As can be seen that the probability of two N decaying in the muon spectrometer is much smaller $\mathcal{P} \sim 1\%$, compared to the probability of two N decaying in the inner-detector, where probability is $\mathcal{P} > 99\%$. This order of magnitude difference in the geometric cut-efficiency is primarily responsible [5] for the reduction in number of 2MSvx signal events. The prospect of detection of 1MSvx events is higher in HL-LHC compared to 2MSvx events, as can be seen by comparing right panel of Fig. 11 and Fig. 12. A maximum of $N_{events} = 3$ events can be obtained with 3 ab^{-1} of data.

We also show the events where one of two Ns decays in the inner-detector and the other N decays in the muon spectrometer, which we refer as MSID event category. The geometric probability for this is somewhat similar to the respective probability of 2MSvx events, as can be seen from Fig. 6. We show the event contours in Fig. 16 assuming 100% kinematic cut-efficiency.

7 Projection for FCC-hh

We consider the same decay channel and signal description as we consider for HL-LHC and present results for $M_{Z'} = 8$ TeV, $g' = 0.1$. The necessary details about the geometry of the inner detector, muon spectrometer that we consider for the analysis has been given in

---

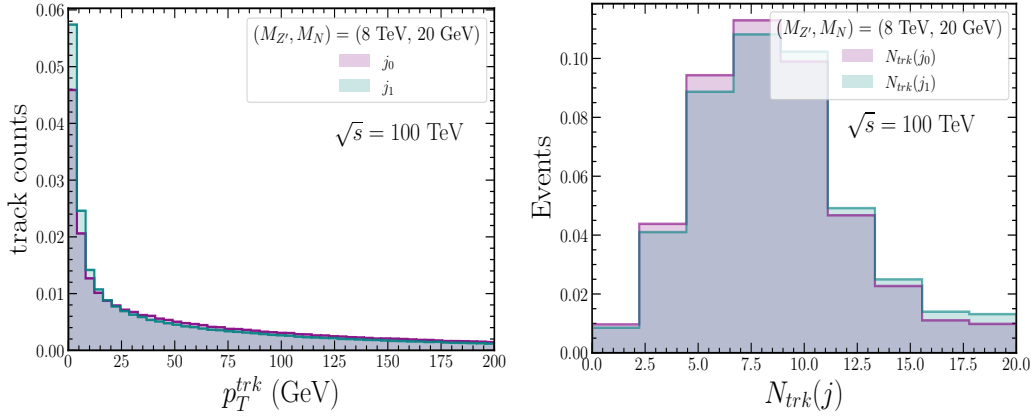[5]The kinematic cut-efficiency is more than 90% for both 2IDvx and 2MSvx events.

Figure 13: Left: p_T of tracks associated to leading and sub-leading jets, relevant for FCC-hh. Right: Number of tracks associated to $j_{0,1}$ for FCC-hh.
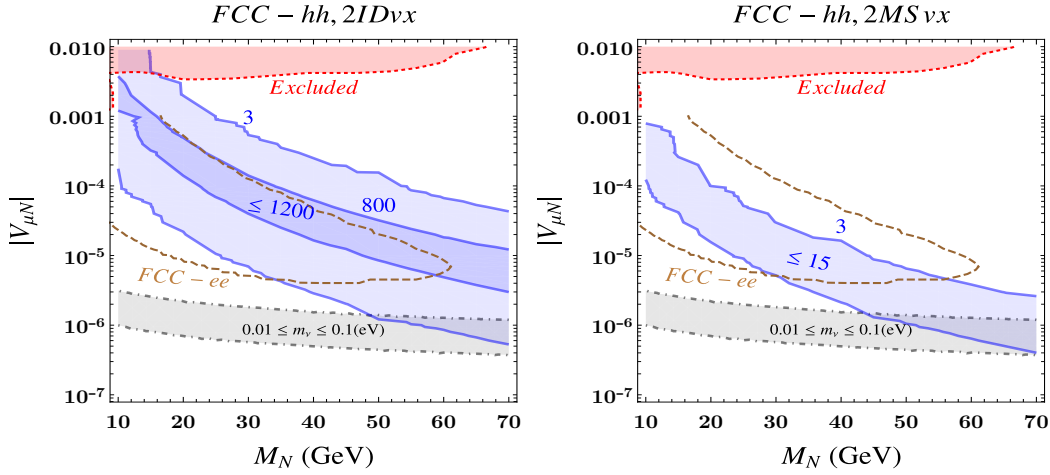

Figure 14: Contours of 2IDvx (left) and 2MSvx (right) events for FCC-hh with $\mathcal{L} = 30\,\text{ab}^{-1}$. The description of the brown dashed line and red shaded region remains the same as given in the previous figures.

Table. 1. We implement similar set of kenematic cuts as used for HL-LHC study in Sec.6. Here we use harder p_T cuts for fat-jet.

7.1 RHN decay signature with IDvx:

We consider two RHN decaying in the inner detector of FCC-hh, for which we use the following sets of cuts,

- *C1:* Both the Ns decay within the detector length $ID_{L_1} = 25$ mm, and $ID_{L_2} = 1550$ mm.

- *C2:* The leading and sub-leading jet $j_{0,1}$ has to satisfy $|\eta(j)| < 4.5$ and $p_T(j) \geq 300$ GeV. A higher p_T cut on the jet p_T will be useful to suppress the SM backgrounds.
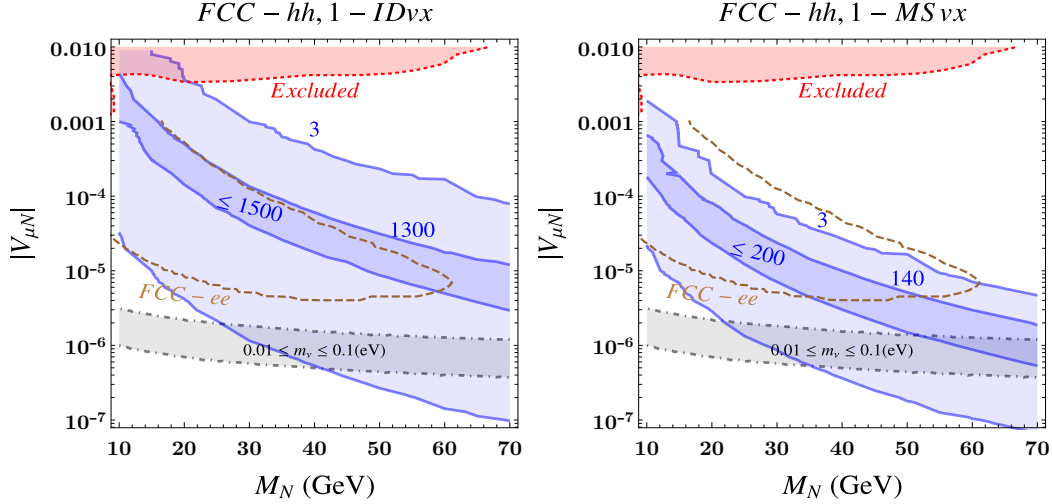
Figure 15: Event contours for 1IDvx (left) and 1MSvx (right) at FCC-hh with $\mathcal{L} = 30\,\mathrm{ab}^{-1}$.

- *C3:* Additionally for each of the $j_{0,1}$, number of associated tracks with $p_T \geq 1\mathrm{GeV}$ and $|\eta| < 2.5$ should satisfy $n_{trk} \geq 4$. We show the distribution of track-p_T and number of tracks in Fig. 13 for $M_N = 20$ GeV. For higher M_N the number of tracks increases further.

- *C4:* Finally we select the events if number of jets $n_j \geq 2$ and the above-mentioned cuts are satisfied for both the leading and sub-leading *fat-jets*. Additionally, similar to the analysis of HL-LHC, we also present the results demanding displaced decay of at least one RHN [6], for which we consider only the geometric cut efficiency.

In the left panel of Figure. 14, we show the contours for 3 and 800 2IDvx events. We show the event contours corresponding to 1IDvx events in the left panel of Fig. 15. For both of these two scenarios, a huge number of events $N_{events} > 1000$ can be observed at FCC-hh with $\mathcal{L} = 30\,\mathrm{ab}^{-1}$.

7.2 Decay vertex in the muon spectrometer (MSvx):

If RHN decays to a $\mu q q'$ in the muon-spectrometer, we implement the following sets of selection cuts:

- *C1:* We demand both the RHN decay occur within the muon spectrometer between the length $MS_{L_1} = 6000$ mm, and $MS_{L_2} = 9000$ mm.

- *C2:* For each of the tracks originating from RHN decay vertex we impose $p_T(track) > 1$ GeV , $|\eta(track)| < 2.7$ and $n_{trk} \geq 4$. Additionally, $\Sigma_{track} P_T(track) > 60$ GeV. These cuts are similar to the cuts that we use for HL-LHC projection.

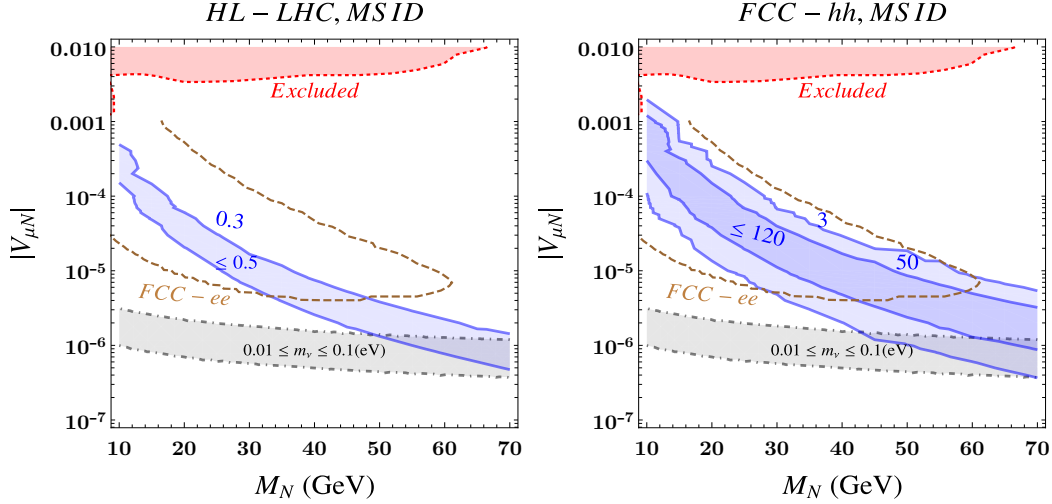[6]For 1IDvx category, we tag displaced decay of one N while the other N can decay anywhere.

Figure 16: Left: Number of events for 1IDvx-1MSvx events at HL-LHC with $\mathcal{L} = 3\,\text{ab}^{-1}$ for $M_{Z'} = 1$ TeV, $g' = 0.003$. Right: The same for FCC-hh with $\mathcal{L} = 30\,\text{ab}^{-1}$ for $M_{Z'} = 8$ TeV, $\text{g}' = 0.1$.

- *C3:* Finally we select the events if two decay vertex and the associated tracks from the vertex satisfy the above selection criterion.

In the right panel of Figure. 14, we show the event contours for two N decaying inside the muon spectrometer. We also show the number of events demanding decay of at least one N in the muon spectrometer in the right panel of Fig. 15, where we take into account only the geometric cut-efficiency. The detection prospect of displaced N decaying in the muon spectrometer is significantly larger for FCC-hh, compared to HL-LHC. This increase in N_{events} occurs due to an increase in the luminosity, and a marginal increase in the cross-section. The kinematic cut-efficiencies are more than 98% for both HL-LHC and FCC-hh MSvx events, and the geometric cut-efficiencies are also somewhat similar (see Fig. 5.2 and Fig. 5.3). Hence, these have little effects in determining increase in the number of events. We also present results for the MSID event category, where one N decays in the ID and the other one decays in the MS. The results are shown in Fig. 16 both of HL-LHC (left panel) and FCC-hh (right panel). A large number of events can be observed at FCC-hh, compared to HL-LHC, with a maximum number of events $N_{events} = 120$ for FCC-hh.

Sentivity reach of $|V_{\mu N}|$: Finally, in Fig. 17, we present the sensitivity reach of $|V_{\mu N}|$ at FCC-hh for different choices of $M_{Z'}$ and g'. We consider few benchmark points with masses $M_{Z'} = 5, 8$ TeV and coupling $g' = 0.1$, as well as, a relatively higher mass $M_{Z'} = 10$ TeV with coupling $g' = 1$. Since our signal contains sufficiently large displaced vertices, hence the SM background polluting the signal would be rather small. In the absence of any background, which we consider in this analysis, following a Poisson distribution only $N_{event} = 3.09$ is required at 95% confidence level. The variation of the sensitivity reach of $|V_{\mu N}|$ w.r.t different choices of M_N has been shown for 2IDvx events (left panel), and for 2MSvx events (right panel). We note that, fixing $M_{Z'}$ and g', overall a smaller value of
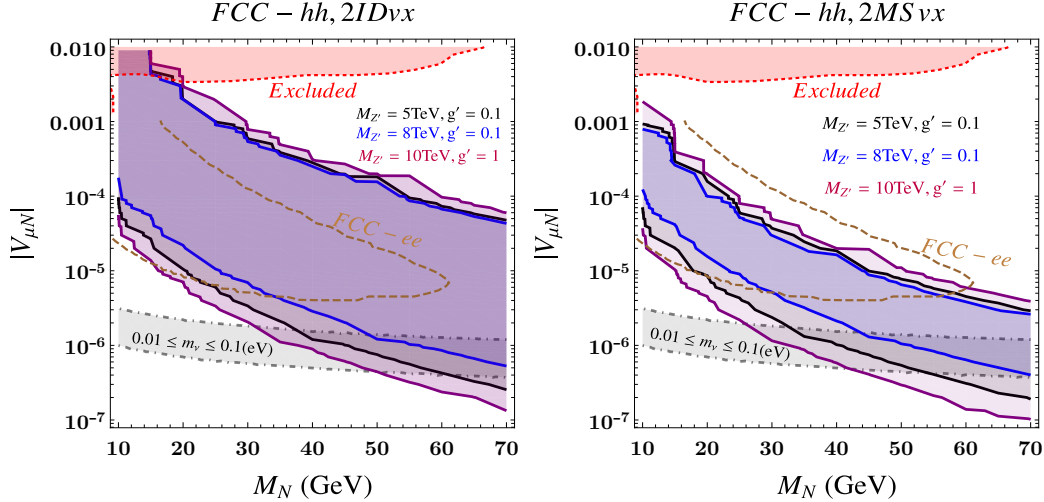
Figure 17: Contours for 3 events for various banchmark at FCC-hh

active-sterile mixing $|V_{\mu N}|$ is required to obtain $N_{event} \sim 3.00$ events for the 2MSvx events, compared to 2IDvx events. This occurs due to a larger decay length of N for its decay into a muon spectrometer. Although the sensitivity reach for $|V_{\mu N}|$ for 2MSvx events have a significant overlap with the sensitivity reach for 2IDvx, however the former has added benefit as 2MSvx events in the muon spectrometer will serve as background free distinctive signal of the model.

8 Conclusion and outlook

The RHN N in the gauged $B - L$ model can be pair-produced at a pp machine via the heavy Z' mediated channel, and give distinctive signatures with displaced vertices. The pair-production of N is independent of active-sterile mixing, instead depends on the $B - L$ gauge coupling g', mass of Z', and mass M_N of N. Hence, even with an active-sterile mixing which is suppressed due to light neutrino mass constraint, fairly large cross-section $\sigma \sim$ fb and even higher can be achieved. We consider a relatively light N with $M_N < M_W$, that satisfies light neutrino mass constraint $m_\nu < 0.1$ eV. For our choice of M_N, the constraint from eV light neutrino mass results in a suppressed active-sterile mixing $|V_{\ell N}| \sim 10^{-6}$. For the considered range of M_N and small $|V_{lN}|$, the RHN undergoes three body decays with the decay vertex considerably displaced from its production vertex. We find that, N undergoes a large displacement $\ell \sim mm$ upto *meter* if M_N varies in between 10-70 GeV. Additionally, due to $M_N \ll M_{Z'}$, the produced N is significantly boosted, resulting in collimated decay products.

We analyse the displaced decay signatures of such a light N that can be probed at the high-luminosity run of the LHC (HL-LHC) with c.m.energy $\sqrt{s} = 14$ TeV and the future pp machine FCC-hh that can operate with c.m.energy $\sqrt{s} = 100$ TeV. Specifically, we consider two scenarios, which are N decays a) within the inner-detector (ID) of the HL-LHC and FCC-hh detectors, and b) within the first few layers of the muon spectrometer (MS). For

the former, N should have proper decay length $\ell \sim$ mm to hundreds of mm, while for later, the decay length should be $\ell \sim$ m. We emphasize that the signal description between a) and b) differ widely. For a detail analysis of the signature, we specifically consider $N \to \mu q q'$ decay mode. For a), i.e., if the decay of N occurs in the ID, the collimated decay products of N result in a displaced *fat-jet*. For this case, we thus analyse model signature with two displaced *fat-jets*, and further extend the analysis to take into account displaced decay of at-least one N. We find that $\mathcal{O}(10)$ displaced *fat-jet* events can be observed at HL-LHC with $3\,\mathrm{ab}^{-1}$ of luminosity, and for FCC-hh, a significantly large number of events $\mathcal{O}(1000)$ can be observed with $\mathcal{L} = 30\,\mathrm{ab}^{-1}$.

For b), i.e., if N decays in the MS, *fat-jet* description can not be used, since energy deposit in the calorimeter, informations about the track in the ID etc are missing, which are being used for the formation of a jet. In this case, we instead perform an analysis that relies on the properties of tracks in the MS. We apply selection cuts on the number of tracks originated from RHN decay, p_T and $|\eta|$, and summation of p_T of the tracks associated with N. We find that for HL-LHC, even after using the full integrated luminosity, the sensitivity reach is significantly low. For FCC-hh, this improves by order of magnitude, as a large number of events $\mathcal{O}(100)$ can be observed with the full integrated luminosity. We also extend the analysis for the case, when one of the N decays in the ID and the other N decays in the MS, for which results are similar to b).

Our proposed signature can potentially be explored for other decay modes of N, including $N \to e q q'$, as well as $N \to \nu q q'$ final states. The final state with electron depends on active sterile mixing $|V_{eN}|$, and hence choosing a large V_{eN} compared to $V_{\mu N}$ will make the contribution from $N \to e q q'$ large. The $N \to \nu q q'$ decay instead depends on all possible $|V_{lN}|$. The final state in addition to displaced *fat-jet* or charged tracks, will also carry missing transverse energy. By applying a veto on MET will hence reduce the contamination from $\nu q q'$ decay mode. A detail analysis of the model signature including both $e q q'$ and $\nu q q'$ decays will be presented elsewhere.

Acknowledgments

References

[1] I. Esteban, M. C. Gonzalez-Garcia, M. Maltoni, T. Schwetz and A. Zhou, *The fate of hints: updated global analysis of three-flavor neutrino oscillations*, *JHEP* **09** (2020) 178, [2007.14792].

[2] R. N. Mohapatra and R. Marshak, *Local B-L Symmetry of Electroweak Interactions, Majorana Neutrinos and Neutron Oscillations*, *Phys. Rev. Lett.* **44** (1980) 1316–1319.

[3] C. Wetterich, *Neutrino Masses and the Scale of B-L Violation*, *Nucl. Phys. B* **187** (1981) 343–375.

[4] H. M. Georgi, S. L. Glashow and S. Nussinov, *Unconventional Model of Neutrino Masses*, *Nucl. Phys. B* **193** (1981) 297–316.

[5] A. Davidson, $B - L$ *as the fourth color within an* $\mathrm{SU}(2)_L \times \mathrm{U}(1)_R \times \mathrm{U}(1)$ *model*, *Phys. Rev. D* **20** (1979) 776.

[6] S. Weinberg, *Baryon and Lepton Nonconserving Processes*, *Phys. Rev. Lett.* **43** (1979) 1566–1570.

[7] F. Wilczek and A. Zee, *Operator Analysis of Nucleon Decay*, *Phys. Rev. Lett.* **43** (1979) 1571–1573.

[8] P. Minkowski, $\mu \to e\gamma$ *at a Rate of One Out of* 10^9 *Muon Decays?*, *Phys. Lett.* **B67** (1977) 421–428.

[9] R. N. Mohapatra and G. Senjanovic, *Neutrino Mass and Spontaneous Parity Nonconservation*, *Phys. Rev. Lett.* **44** (1980) 912.

[10] T. Yanagida, *Horizontal Symmetry and Masses of Neutrinos*, *Conf. Proc.* **C7902131** (1979) 95–99.

[11] M. Gell-Mann, P. Ramond and R. Slansky, *Complex Spinors and Unified Theories*, *Conf. Proc.* **C790927** (1979) 315–321, [1306.4669].

[12] J. Schechter and J. W. F. Valle, *Neutrino Masses in SU(2) × U(1) Theories*, *Phys. Rev.* **D22** (1980) 2227.

[13] R. N. Mohapatra and R. E. Marshak, *Local $b - l$ symmetry of electroweak interactions, majorana neutrinos, and neutron oscillations*, *Phys. Rev. Lett.* **44** (May, 1980) 1316–1319.

[14] C. Wetterich, *Neutrino masses and the scale of b-l violation*, *Nuclear Physics B* **187** (1981) 343–375.

[15] F. F. Deppisch, W. Liu and M. Mitra, *Long-lived Heavy Neutrinos from Higgs Decays*, *JHEP* **08** (2018) 181, [1804.04075].

[16] S. Antusch, E. Cazzato and O. Fischer, *Sterile neutrino searches via displaced vertices at LHCb*, *Phys. Lett. B* **774** (2017) 114–118, [1706.05990].

[17] G. Cottin, J. C. Helo and M. Hirsch, *Displaced vertices as probes of sterile neutrino mixing at the LHC*, *Phys. Rev. D* **98** (2018) 035012, [1806.05191].

[18] M. Drewes and J. Hajer, *Heavy Neutrinos in displaced vertex searches at the LHC and HL-LHC*, *JHEP* **02** (2020) 070, [1903.06100].

[19] A. Abada, N. Bernal, M. Losada and X. Marcano, *Inclusive Displaced Vertex Searches for Heavy Neutral Leptons at the LHC*, *JHEP* **01** (2019) 093, [1807.10024].

[20] J. Liu, Z. Liu, L.-T. Wang and X.-P. Wang, *Seeking for sterile neutrinos with displaced leptons at the LHC*, *JHEP* **07** (2019) 159, [1904.01020].

[21] W. Liu, S. Kulkarni and F. F. Deppisch, *Heavy Neutrinos at the FCC-hh in the* $U(1)_{B-L}$ *Model*, 2202.07310.

[22] G. M. Pruna, *Phenomenology of the minimal $B - L$ Model: the Higgs sector at the Large Hadron Collider and future Linear Colliders.* PhD thesis, Southampton U., 2011. 1106.4691.

[23] ATLAS collaboration, G. Aad et al., *Search for high-mass dilepton resonances using 139 fb^{-1} of pp collision data collected at $\sqrt{s}$ =13 TeV with the ATLAS detector, Phys. Lett. B* **796** (2019) 68–87, [1903.06248].

[24] CMS collaboration, A. M. Sirunyan et al., *Search for resonant and nonresonant new phenomena in high-mass dilepton final states at $\sqrt{s}$ = 13 TeV, JHEP* **07** (2021) 208, [2103.02708].

[25] SLAC E158 collaboration, P. L. Anthony et al., *Observation of parity nonconservation in Moller scattering, Phys. Rev. Lett.* **92** (2004) 181602, [hep-ex/0312035].

[26] ATLAS collaboration, F. Rühr, *Prospects for BSM searches at the high-luminosity LHC with the ATLAS detector, Nucl. Part. Phys. Proc.* **273-275** (2016) 625–630.

[27] C. Helsens, D. Jamin, M. L. Mangano, T. G. Rizzo and M. Selvaggi, *Heavy resonances at energy-frontier hadron colliders, Eur. Phys. J. C* **79** (2019) 569, [1902.11217].

[28] G. Cacciapaglia, C. Csaki, G. Marandella and A. Strumia, *The Minimal Set of Electroweak Precision Parameters, Phys. Rev. D* **74** (2006) 033011, [hep-ph/0604111].

[29] LEP, ALEPH, DELPHI, L3, OPAL, LEP ELECTROWEAK WORKING GROUP, SLD ELECTROWEAK GROUP, SLD HEAVY FLAVOR GROUP collaboration, t. S. Electroweak, *A Combination of preliminary electroweak measurements and constraints on the standard model*, hep-ex/0312023.

[30] M. Carena, A. Daleo, B. A. Dobrescu and T. M. P. Tait, *Z$'$ gauge bosons at the Tevatron, Phys. Rev. D* **70** (2004) 093009, [hep-ph/0408098].

[31] CMS collaboration, A. Tumasyan et al., *Search for long-lived heavy neutral leptons with displaced vertices in proton-proton collisions at $\sqrt{s}$ =13 TeV*, 2201.05578.

[32] CMS collaboration, *Search for long-lived heavy neutral leptons with displaced vertices in pp collisions at $\sqrt{s}$ = 13 TeV with the CMS detector*, .

[33] ATLAS collaboration, M. Aaboud et al., *Search for heavy Majorana or Dirac neutrinos and right-handed W gauge bosons in final states with two charged leptons and two jets at $\sqrt{s}$ = 13 TeV with the ATLAS detector, JHEP* **01** (2019) 016, [1809.11105].

[34] CMS collaboration, A. M. Sirunyan et al., *Search for heavy Majorana neutrinos in same-sign dilepton channels in proton-proton collisions at $\sqrt{s}$ = 13 TeV, JHEP* **01** (2019) 122, [1806.10905].

[35] CMS collaboration, A. Tumasyan et al., *Search for a right-handed W boson and a heavy neutrino in proton-proton collisions at $\sqrt{s}$ = 13 TeV*, 2112.03949.

[36] ATLAS COLLABORATION collaboration, *Search for exotic decays of the Higgs boson into long-lived particles in pp collisions at $\sqrt{s}$ = 13 TeV using displaced vertices in the ATLAS inner detector*, tech. rep., CERN, Geneva, Jul, 2021.

[37] CMS collaboration, *Search for Higgs boson decays into long-lived particles in associated Z boson production*, .

[38] CMS COLLABORATION collaboration, *Search for long-lived particles decaying to displaced leptons in proton-proton collisions at $\sqrt{s}$ = 13 TeV*, tech. rep., CERN, Geneva, 2021.

[39] CMS collaboration, A. M. Sirunyan et al., *Search for long-lived particles using displaced jets in proton-proton collisions at $\sqrt{s}$ = 13 TeV, Phys. Rev. D* **104** (2021) 012015, [2012.01581].

[40] ATLAS COLLABORATION collaboration, *Search for events with a pair of displaced vertices from long-lived neutral particles decaying into hadronic jets in the ATLAS muon spectrometer in pp collisions at $\sqrt{s} = 13$ TeV*, tech. rep., CERN, Geneva, Jul, 2021.

[41] ATLAS collaboration, G. Aad et al., *Search for long-lived neutral particles produced in pp collisions at $\sqrt{s} = 13$ TeV decaying into displaced hadronic jets in the ATLAS inner detector and muon spectrometer*, *Phys. Rev. D* **101** (2020) 052013, [1911.12575].

[42] ATLAS collaboration, M. Aaboud et al., *Search for long-lived particles produced in pp collisions at $\sqrt{s} = 13$ TeV that decay into displaced hadronic jets in the ATLAS muon spectrometer*, *Phys. Rev. D* **99** (2019) 052005, [1811.07370].

[43] CMS collaboration, A. Tumasyan et al., *Search for long-lived particles decaying in the CMS endcap muon detectors in proton-proton collisions at $\sqrt{s} = 13$ TeV*, 2107.04838.

[44] K. Bondarenko, A. Boyarsky, D. Gorbunov and O. Ruchayskiy, *Phenomenology of GeV-scale Heavy Neutral Leptons*, *JHEP* **11** (2018) 032, [1805.08567].

[45] A. Alloul, N. D. Christensen, C. Degrande, C. Duhr and B. Fuks, *FeynRules 2.0 - A complete toolbox for tree-level phenomenology*, *Comput. Phys. Commun.* **185** (2014) 2250–2300, [1310.1921].

[46] N. D. Christensen and C. Duhr, *FeynRules - Feynman rules made easy*, *Comput. Phys. Commun.* **180** (2009) 1614–1641, [0806.4194].

[47] C. Degrande, C. Duhr, B. Fuks, D. Grellscheid, O. Mattelaer and T. Reiter, *UFO - The Universal FeynRules Output*, *Comput. Phys. Commun.* **183** (2012) 1201–1214, [1108.2040].

[48] J. Alwall, R. Frederix, S. Frixione, V. Hirschi, F. Maltoni, O. Mattelaer et al., *The automated computation of tree-level and next-to-leading order differential cross sections, and their matching to parton shower simulations*, *JHEP* **07** (2014) 079, [1405.0301].

[49] "Feynrulesdatabase." https://feynrules.irmp.ucl.ac.be/wiki/B-L-SM.

[50] A. Buckley, J. Ferrando, S. Lloyd, K. Nordström, B. Page, M. Rüfenacht et al., *LHAPDF6: parton density access in the LHC precision era*, *Eur. Phys. J. C* **75** (2015) 132, [1412.7420].

[51] T. Sjöstrand, S. Ask, J. R. Christiansen, R. Corke, N. Desai, P. Ilten et al., *An Introduction to PYTHIA 8.2*, *Comput. Phys. Commun.* **191** (2015) 159–177, [1410.3012].

[52] M. Cacciari, G. P. Salam and G. Soyez, *FastJet User Manual*, *Eur. Phys. J. C* **72** (2012) 1896, [1111.6097].

[53] Y. L. Dokshitzer, G. D. Leder, S. Moretti and B. R. Webber, *Better jet clustering algorithms*, *JHEP* **08** (1997) 001, [hep-ph/9707323].

[54] A. Buckley, P. Ilten, D. Konstantinov, L. Lönnblad, J. Monk, W. Pokorski et al., *The HepMC3 event record library for Monte Carlo event generators*, *Comput. Phys. Commun.* **260** (2021) 107310, [1912.08005].

[55] J. Alwall et al., *A Standard format for Les Houches event files*, *Comput. Phys. Commun.* **176** (2007) 300–304, [hep-ph/0609017].

[56] ATLAS collaboration, M. Aaboud et al., *Search for long-lived neutral particles in pp collisions at $\sqrt{s} = 13$ TeV that decay into displaced hadronic jets in the ATLAS calorimeter*, *Eur. Phys. J. C* **79** (2019) 481, [1902.03094].

[57] FCC collaboration, A. Abada et al., *FCC-hh: The Hadron Collider: Future Circular Collider Conceptual Design Report Volume 3*, *Eur. Phys. J. ST* **228** (2019) 755–1107.

[58] CMS collaboration, A. M. Sirunyan et al., *Inclusive search for a highly boosted Higgs boson decaying to a bottom quark-antiquark pair*, *Phys. Rev. Lett.* **120** (2018) 071802, [1709.05543].

[59] FCC-ee study Team collaboration, A. Blondel, E. Graverini, N. Serra and M. Shaposhnikov, *Search for Heavy Right Handed Neutrinos at the FCC-ee*, *Nucl. Part. Phys. Proc.* **273-275** (2016) 1883–1890, [1411.5230].

[60] P. D. Bolton, F. F. Deppisch and P. S. Bhupal Dev, *Neutrinoless double beta decay versus other probes of heavy sterile neutrinos*, *JHEP* **03** (2020) 170, [1912.03058].

[61] ATLAS collaboration, G. Aad et al., *Search for heavy neutral leptons in decays of W bosons produced in 13 TeV pp collisions using prompt and displaced signatures with the ATLAS detector*, *JHEP* **10** (2019) 265, [1905.09787].

[62] CMS collaboration, A. M. Sirunyan et al., *Search for heavy neutral leptons in events with three charged leptons in proton-proton collisions at $\sqrt{s}$ = 13 TeV*, *Phys. Rev. Lett.* **120** (2018) 221801, [1802.02965].

[63] ATLAS collaboration, M. Aaboud et al., *Search for a right-handed gauge boson decaying into a high-momentum heavy neutrino and a charged lepton in pp collisions with the ATLAS detector at $\sqrt{s}$ = 13 TeV*, *Phys. Lett. B* **798** (2019) 134942, [1904.12679].

[64] S. Banerjee, C. Englert, M. L. Mangano, M. Selvaggi and M. Spannowsky, *hh + jet production at 100 TeV*, *Eur. Phys. J. C* **78** (2018) 322, [1802.01607].

[65] M. J. Dolan, C. Englert and M. Spannowsky, *Higgs self-coupling measurements at the LHC*, *JHEP* **10** (2012) 112, [1206.5001].